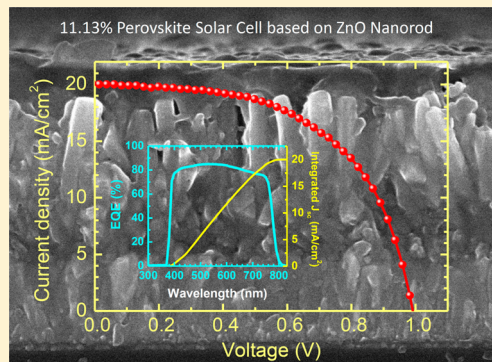


11% Efficient Perovskite Solar Cell Based on ZnO Nanorods: An Effective Charge Collection System

Dae-Yong Son, Jeong-Hyeok Im, Hui-Seon Kim, and Nam-Gyu Park*

School of Chemical Engineering and Department of Energy Science, Sungkyunkwan University (SKKU), Suwon, Gyeonggi 440-746, Korea

ABSTRACT: A perovskite solar cell based on ZnO nanorods was prepared, and its photovoltaic performance was investigated. ZnO nanorods were grown on the ZnO seed layer from solution, and their diameters and lengths were controlled by precursor concentration and growth time. $\text{CH}_3\text{NH}_3\text{PbI}_3$ perovskite infiltrated ZnO nanorods showed a power conversion efficiency of 11.13% with short-circuit current density J_{sc} of 20.08 mA/cm^2 , open-circuit voltage V_{oc} of 991 mV and fill factor of 0.56. Square spectral feature of external quantum efficiency (EQE) was observed, where EQE exceeded 80% in almost the entire wavelength range from 400 to 750 nm, and the integrated current density of 20.03 mA/cm^2 calculated from EQE data was in good agreement with the observed J_{sc} . Compared to the perfect spectral response of ZnO nanorods, a perovskite solar cell based on TiO_2 nanorods exhibited an integrated current density (16 mA/cm^2) much lower than the measured J_{sc} (20.9 mA/cm^2). In addition, time-limited photocurrent response under 530 and 700 nm monochromatic beams at 10 Hz showed that device signal amplitude, associated with charge collection, was rapidly saturated for the ZnO nanorod-based device whereas charge collection was not fully detected for the TiO_2 nanorod-based device because of slow collection rate. The current results suggest that ZnO nanorod is an effective charge collection system in $\text{CH}_3\text{NH}_3\text{PbI}_3$ based perovskite solar cells.



INTRODUCTION

Perovskite solar cells based on organolead halide light harvester have recently attracted much attention because of superb photovoltaic performance and very inexpensive technology. The first attempt of using $\text{CH}_3\text{NH}_3\text{PbX}_3$ ($X = \text{Br}$ or I) as light harvester was made in dye-sensitized liquid-type solar cells, which resulted in power conversion efficiency (PCE) of 3.1–3.8%.¹ PCE was significantly improved to 6.5% by optimizing the concentration of the $\text{CH}_3\text{NH}_3\text{PbI}_3$ coating solution, perovskite annealing temperature, and electrolyte composition.² However, the perovskite light harvester suffers from liquid-type dye-sensitized solar cell because it tends to easily dissolve in the polar liquid electrolyte. This problem has been solved by replacing the liquid electrolyte with solid hole conductor. All-solid-state solar cell comprising $\text{CH}_3\text{NH}_3\text{PbI}_3$ nanodots deposited on TiO_2 surface demonstrated a PCE of 9.7%, along with excellent long-term stability.³ It was also confirmed that the perovskite solar cell could work well even without a mesoporous TiO_2 film, where a thin, continuous $\text{CH}_3\text{NH}_3\text{PbI}_2\text{Cl}$ layer formed on the Al_2O_3 surface showed a PCE of 10.9%.⁴ Recent progress pushed PCE of perovskite solar cell up to 15%.^{5,6} Thanks to the high open-circuit voltage V_{oc} of perovskite solar cell exceeding 1 V, a PCE of 20% is predicted from perovskite solar cell,^{7,8} which indicates that organometal halide perovskite is a very promising solar cell material.

There are two branches in developing perovskite solar cell; one is based on electron-injecting nanostructured oxide layer,

and the other is based on nonelectron-injecting scaffold layer (meso-superstructure) or *pn* junction type planar structure. For the case of the electron-injecting oxide system, except for the TiO_2 nanoparticles, one-dimensional TiO_2 ^{9–11} and ZnO ^{12,13} were investigated. Although electron transport in ZnO was observed to be faster than that in TiO_2 ,¹³ photovoltaic performances of ZnO nanorod-based perovskite solar cells were inferior to those of TiO_2 nanorod-based solar cells. This might be due to nonoptimized ZnO nanorods.

Here, we report high-efficiency ZnO nanorod-based perovskite solar cells. Diameter and length of the solution-grown ZnO nanorods are controlled by varying the solution concentration and immersion time. PCE of 11.13% is achieved using 1 μm long ZnO nanorods (diameter of about 80 nm) in the absence of a compact TiO_2 blocking layer. The photovoltaic performance, especially external quantum efficiency (EQE) spectral response is compared between ZnO nanorods and TiO_2 nanorods.

EXPERIMENTAL SECTION

ZnO nanorods were grown based on the methods described elsewhere.^{14–16} Laser-patterned fluorine-doped tin oxide

Special Issue: Michael Grätzel Festschrift

Received: December 18, 2013

Revised: February 28, 2014

Published: March 7, 2014

(FTO) glass (Pilkington, TEC-8, 8 Ω/sq) was cleaned with ethyl alcohol, water, and acetone several times. The cleaned FTO glass samples were further treated with UVO for 15 min to get rid of organic materials. The ZnO seed layer was first prepared as follows. A 5 mM ethanol solution of zinc acetate dihydrate ($\text{Zn}(\text{CH}_3\text{COO})_2 \cdot 2\text{H}_2\text{O}$, Aldrich, 98%) was spin-coated on the cleaned FTO glass at a spinning rate of 2000 rpm for 20 s with a 10 s wait time, which was followed by annealing at 150 °C for 15 min. This was repeated 3 times, and finally the ZnO seed layer was annealed at 350 °C for 15 min. The solution for growing ZnO nanorods was prepared by dissolving equimolar zinc nitrate hexahydrate ($\text{Zn}(\text{NO}_3)_2 \cdot 6\text{H}_2\text{O}$, Aldrich, 98%) and hexamethylenetetramine (HMTA, Aldrich, 99%) in deionized (DI) water. The solution concentration was varied from 20 to 35 mM for controlling the diameter of the ZnO nanorods. The ZnO seed layer deposited FTO glass was immersed in the solution, where the FTO side was placed facedown, and the beaker was kept at 90 °C for 90, 120, 150, and 180 min. Change in the immersion time at a given concentration can control the length of the ZnO nanorods. The ZnO nanorod film was rinsed with DI water and ethyl alcohol several times. Finally, the film was annealed at 450 °C for 30 min. For comparison, rutile TiO₂ nanorods were prepared according to the method reported elsewhere.⁹ TiO₂ nanorods were grown on a dense TiO₂ layer coated FTO glass. The dense TiO₂ layer was prepared according to the method described in a previous report.³ In brief, 20 mL of 37% hydrochloric acid and 20 mL of DI water were mixed and stirred for 5 min, to which 0.7 mL of titanium(IV) *n*-butoxide (99%, Aldrich) was added; the mixture was then stirred for 10 min. The acidic titanium alkoxide solution was poured into a Teflon liner in which the compact TiO₂ coated FTO glass was immersed, where the FTO side was placed facedown. A 100 mL capacity autoclave was kept in a preheated oven at 170 °C for 210 min. After being cooled, the TiO₂ nanorod film was rinsed with DI water and ethyl alcohol several times and then annealed at 550 °C for 1 h.

$\text{CH}_3\text{NH}_3\text{PbI}_3$ was deposited in the ZnO nanorod or the TiO₂ nanorod film using a two-step method.⁵ A 1 M PbI₂ solution was prepared by dissolving 2.33 g of PbI₂ in 5 mL of *N,N*-dimethylformamide (DMF). The solution was kept at 70 °C for 2 h. A $\text{CH}_3\text{NH}_3\text{I}$ solution was prepared by dissolving 0.05 g of $\text{CH}_3\text{NH}_3\text{I}$ in 5 mL of 2-propanol (0.063 M), where $\text{CH}_3\text{NH}_3\text{I}$ was prepared by reacting CH_3NH_2 with aqueous HI.² A 100 μL portion of the PbI₂ solution was dropped on the ZnO or TiO₂ nanorod-coated 2.5 × 2.5 cm² FTO substrate; the substrate was spun immediately at 3000 rpm for 20 s and dried at 100 °C for 10 min. After the substrate cooled, 200 μL of $\text{CH}_3\text{NH}_3\text{I}$ solution was dropped on the substrate; a wait time of 20 s was observed, and then the sample was spun at 2000 rpm for 20 s and dried at 100 °C for 10 min. The hole transporting layer was formed by spin-coating the 2,2',7,7'-tetrakis(*N,N*-p-dimethoxyphenylamino)-9,9'-spirobifluorene (spiro-MeOTAD) solution at 3000 rpm for 30 s, where 72.3 mg of spiro-MeOTAD was mixed with 28.8 μL of 4-*tert*-butylpyridine and 17.5 μL of lithium bis(trifluoromethylsulfonyl) imide (LiTFSI) solution (520 mg of LiTFSI in 1 mL of acetonitrile), and those mixture were dissolved in 1 mL of chlorobenzene. Finally ca. 60 nm of Au was deposited using a thermal evaporator at a deposition rate of 1.5 Å/s.

Photocurrent density–voltage (*J*–*V*) characteristics were measured under AM 1.5G one sun (100 mW/cm²) illumination by using a solar simulator (Oriel Sol 3A class AAA) equipped

with a 450 W xenon lamp (Newport 6279NS) and a Keithley 2400 source meter. The light intensity was adjusted by a NREL-calibrated Si solar cell with a KG-2 filter. During the measurements, the cell was covered with a mask having an aperture. External quantum efficiency (EQE) was measured using an EQE system (PV Measurements Inc.). The source light for generating the monochromatic beam was a 75 W xenon lamp (USHIO, Japan). EQE data acquisition was carried out at DC mode.¹⁷ Time-limited current response was recorded at 10 Hz under 530 and 700 nm monochromatic beams. Time constants for charge recombination was measured with a weak laser pulse at 532 nm superimposed on a relatively large bias illumination at 680 nm using a transient photocurrent–voltage measurement setup described elsewhere.¹⁸ Transient photocurrent or photovoltage measurement was performed with a small light perturbation, where probe light was incident over the steady-state charge induced by a bias light. The intensity of the probe light was varied by a neutral density filter corresponding to that of bias light that generates steady-state charge. The light intensity of the probe laser was much less than that of the bias light. Probe light of 0.38, 0.3, 0.147, and 0.045 nW was incident over the bias light of 14.99, 9.99, 2.59, 0.207 mW, respectively. Therefore, the collected charge induced by the probe laser was maintained below 0.1% of the steady-state charge. Although the absorption of the wavelength of the probe laser, 535 nm, is much more favored than that of the 680 nm of the bias light, the 0.1% value is still reliable for avoiding other effects. The incident charge by probe light rapidly decreased, showing first-order exponential decay. The time constant *t* was obtained by fitting to the measured data using the relation $y = y_0 + A\exp(-x/t)$.¹⁹

X-ray diffraction data were collected using a Philips PW 1050 diffractometer under graphite-monochromated Cu K α radiation ($\lambda = 1.54184$ Å). Surface and cross-sectional morphologies were investigated using scanning electron microscopy (SEM, JSM-7600F, JEOL).

RESULTS AND DISCUSSION

Diameter *d* of ZnO nanorod is controlled by changing the precursor concentration. Figure 1 shows that average *d* increases from 54 to 61, 73, and 82 nm as the precursor concentration increases from 20 to 25, 30, and 35 mM, respectively, where the immersion time is fixed at 180 min at 90 °C. Length of the grown ZnO nanorods is about 1 μm regardless of concentration, which indicates that change in the precursor concentration at the fixed immersion time can affect only the diameter of the hexagonal ZnO nanorods. The rate of increase in diameter of the ZnO nanorods is estimated to be approximately 2.4 nm/mM.

Length of ZnO nanorods can also be varied when the immersion time changes at the fixed concentration. Figure 2 shows that average length of the ZnO nanorods increases from 440 nm to 620 nm, 820 nm, and 1 μm as the immersion time *t* increases from 90 to 120, 150, and 180 min, respectively, at the precursor concentration of 35 mM. Length *l* of ZnO nanorods grows by the relation $l = 6.27t - 126$, which indicates that growth rate is 6.27 nm/min and a warming-up time of about 20 min is required.

The X-ray diffraction pattern in Figure 3 shows the highly oriented nature of ZnO nanorods. The strongest (002) peak reflects that *c*-axis elongated nanorods are oriented normal to the FTO substrate,^{20,21} compared to the prominent (101) peak for the polycrystalline powder ZnO.²²

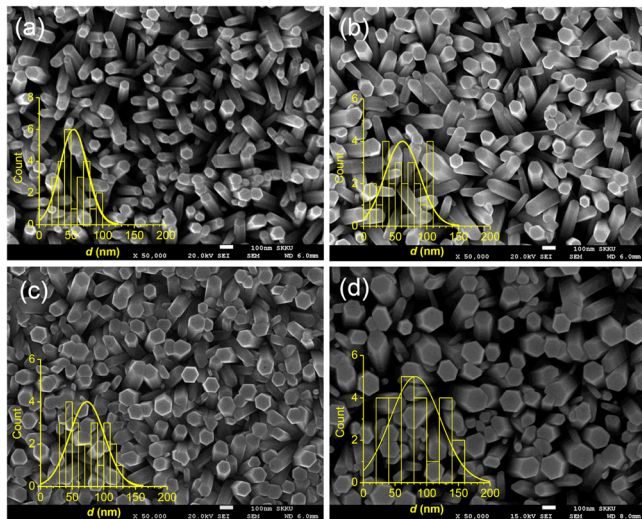


Figure 1. Surface SEM images of hexagonal ZnO nanorods grown at (a) 20, (b) 25, (c) 30, and (d) 35 mM of the precursor solution containing equimolar zinc nitrate hexahydrate and hexamethylenetetramine. The ZnO seed layer deposited FTO substrates were immersed in the precursor solution at 90 °C for 180 min. Insets represent distribution of diameters of ZnO nanorods.

Perovskite solar cells were prepared using the ZnO nanorods approximately 82 nm wide and 1 μm long that were grown at 90 °C for 180 min from the 35 mM precursor solution. The fabrication procedure of perovskite solar cell based on the ZnO nanorod electrode is depicted in Figure 4. $\text{CH}_3\text{NH}_3\text{PbI}_3$ is formed by intercalation reaction of $\text{CH}_3\text{NH}_3\text{I}$ in the layered PbI_2 .⁵ PbI_2 is formed first in the ZnO nanorod film by a spin-coating method, which is followed by spin-coating the $\text{CH}_3\text{NH}_3\text{I}$ solution. A concentration of the $\text{CH}_3\text{NH}_3\text{I}$ solution (~0.063 M) lower than that of the PbI_2 solution (~1 M) is used in order to form the perovskite phase immediately. By differentiating spin-coating conditions between $\text{CH}_3\text{NH}_3\text{I}$ and PbI_2 , a pure perovskite phase can be obtained as confirmed by X-ray diffraction pattern showing no PbI_2 peaks after spin-coating of $\text{CH}_3\text{NH}_3\text{I}$ (Figure 5). Finally, thermal evaporation of Au follows spiro-MeOTAD deposition.

Figure 6 shows cross-sectional and surface SEM images of the bare ZnO nanorods, $\text{CH}_3\text{NH}_3\text{PbI}_3$ -deposited ZnO nanorods, and the full cell. In the bare ZnO nanorod electrode in Figure 6a, the compact ZnO seed layer is seen to some extent between the ZnO nanorods and FTO. This ZnO seed layer is expected to play a role in protecting direct contact between FTO and spiro-MeOTAD. Our two-step spin-coating technology leads to formation of an overlayer (capping layer) of the

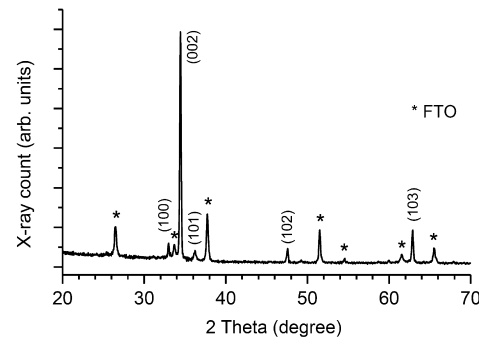


Figure 3. X-ray diffraction pattern as a function of 2θ for the ZnO nanorods grown at 90 °C for 180 min from the 35 mM precursor solution. Asterisks denote FTO substrate peaks.

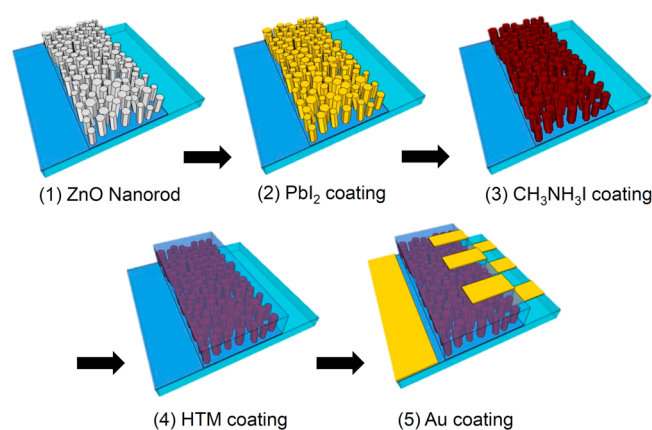


Figure 4. Fabrication procedure of perovskite solar cell based on the ZnO nanorod electrode.

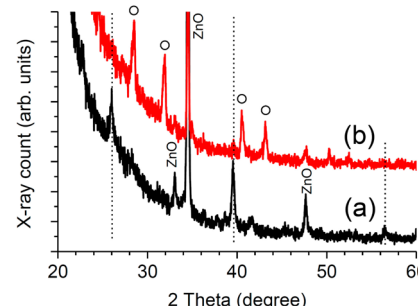


Figure 5. X-ray diffraction pattern for (a) PbI_2 spin-coated ZnO nanorod film on FTO and (b) $\text{CH}_3\text{NH}_3\text{I}$ spin-coated PbI_2 infiltrated ZnO nanorods on FTO. Dotted lines represent PbI_2 characteristic peaks and empty circles represent $\text{CH}_3\text{NH}_3\text{PbI}_3$ perovskite peaks.

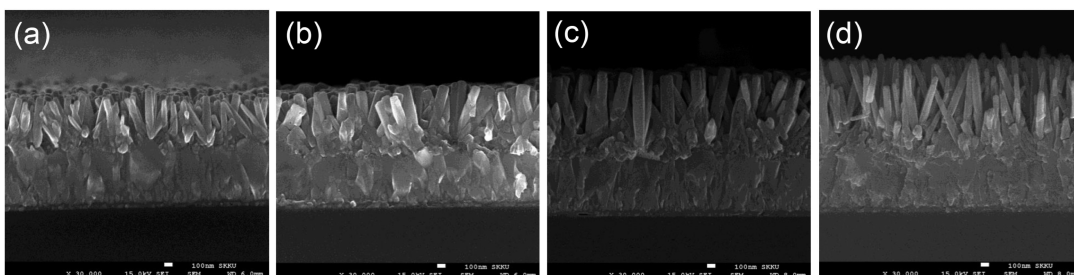


Figure 2. Cross-sectional SEM images of ZnO nanorod grown for (a) 90, (b) 120, (c) 150, and (d) 180 min at the precursor concentration of 35 mM.

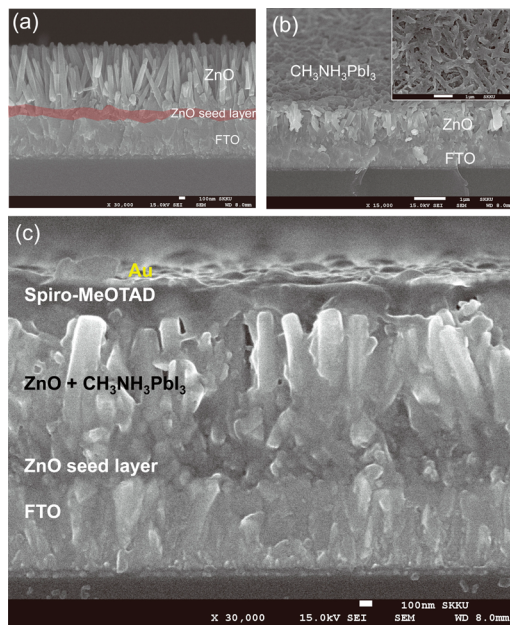


Figure 6. SEM images of (a) bare ZnO nanorod grown on FTO substrate, (b) CH₃NH₃PbI₃-deposited ZnO nanorods, and (c) full cell. Inset in (b) is surface SEM image of the CH₃NH₃PbI₃ capping layer.

CH₃NH₃PbI₃ perovskite on the ZnO nanorod film as can be seen in Figure 6b. Voids are partly found in the ZnO nanorod film, indicative of incomplete pore filling with the perovskite. The capping layer looks fibrous. From the cross section of the full cell in Figure 6c it is noted that spiro-MeOTAD can be found in part in the ZnO nanorods, which implies that the pores in the ZnO nanorod film are not fully filled with the perovskite.

Photovoltaic performance is investigated and displayed in Figure 7. The ZnO nanorod-based perovskite solar cell demonstrates short-circuit current density J_{sc} of 20.08 mA/cm², open-circuit voltage V_{oc} of 991 mV, fill factor (FF) of 0.56 and power conversion efficiency (PCE) of 11.13% at AM 1.5G one sun (100 mW/cm²) illumination, which is by far the highest efficiency for the ZnO nanorod-based dye-sensitized and perovskite solar cells. ZnO nanorods were applied for perovskite solar cells; however, they demonstrated relatively low PCEs of 5%¹³ and 8.9%.¹² EQE spectral shape is close to full-conversion as shown in Figure 7b. EQE already reaches over 77% at wavelengths as short as 400 nm, maximizes its value at 85% at 530 nm, and retains 80% up to 700 nm. Even at a long wavelength of 760 nm, EQE is as high as 70%. The integrated J_{sc} calculated from the EQE data is 20.03 mA/cm², which agrees well with the measured J_{sc} . The light harvesting efficiency (LHE) and the absorbed photon-to-current conversion efficiency (APCE) are estimated based on LHE = $(1 - R)(1 - 10^{-A})$ and APCE = EQE/LHE, where A and R represent absorbance and reflectance, respectively.²³ The spectral shape of LHE in Figure 7c is consistent with that of two-step deposited perovskite on mesoporous TiO₂ film,⁵ but perovskite on the ZnO nanorod shows higher LHE (80% at 750 nm vs 60% at 750 nm in ref 5). This indicates that the present ZnO nanorod system is beneficial for utilizing long wavelength light, which is also confirmed by APCE in Figure 7d.

In previous reports,^{9,13} photovoltaic performance was better for the shorter ZnO or TiO₂ nanorod, where perovskite was

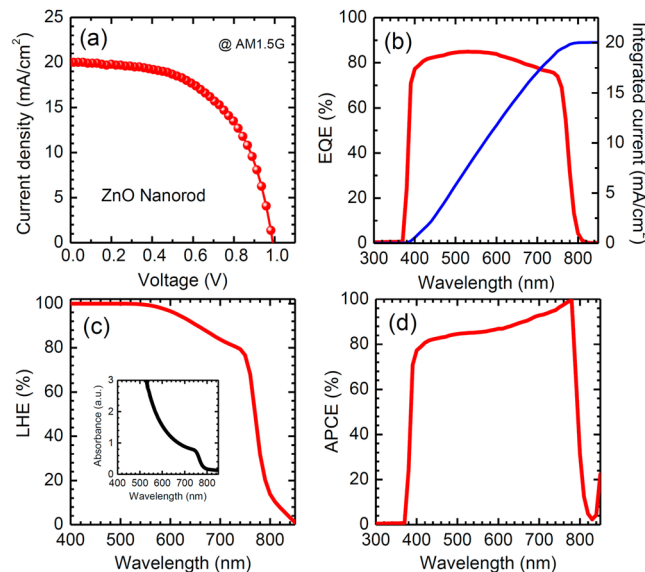


Figure 7. (a) Current density–voltage curve and (b) external quantum efficiency (EQE) spectrum together with EQE data-based integrated current density of the perovskite solar cell based on ZnO nanorod (82 nm wide and 1 μ m long) film. Active area was 0.197 cm². (c) Light-harvesting efficiency (LHE) of the perovskite-coated ZnO nanorod film on FTO. Inset shows absorption spectrum. (d) Absorbed photon-to-current conversion efficiency (APCE) spectrum.

prepared by one-step spin-coating. By using a one-step coating method, pores of oxide film would not be fully filled with perovskite and as a result spiro-MeOTAD should be infiltrated into the pores. Increase in the spiro-MeOTAD layer was therefore accompanied by an increase in ZnO or TiO₂ nanorod length, which can deteriorate photovoltaic performance because of the limiting of hole diffusion in the increased spiro-MeOTAD layer. In contrast to the one-step coating method, the two-step coating procedure in this study results in pore-filling of perovskite, which can control the layer thickness of spiro-MeOTAD for optimal hole diffusion length. In addition, increase in nanorod length improves the absorbance of perovskite (Figure 8c) owing to the increased overall thickness of the perovskite layer (Figure 8d–f). The highest photovoltaic performance is therefore observed from 1000 nm long ZnO nanorods among the studied lengths from 600 to 1000 nm. Figure 8a,b confirms that photocurrent and EQE increase with increasing ZnO nanorod length because of the increased absorbance as shown in Figure 8c.

We compare the photovoltaic performance of the ZnO nanorod-based perovskite solar cell and the rutile TiO₂ nanorod-based solar cell. Figure 9 shows J – V curve, EQE and APCE spectra of TiO₂ nanorod-based perovskite solar cell along with LHE of perovskite coated TiO₂ nanorod film, and cross-sectional SEM images of bare TiO₂ nanorods and full cell. Length of the solution-grown TiO₂ nanorods is about 1 μ m, and their width is 80–90 nm, as can be seen in Figure 9e. TiO₂ compact layer is clearly seen between TiO₂ nanorods and FTO. A thin spiro-MeOTAD HTM layer is formed over the TiO₂ nanorod film (Figure 9f). Two-step spin coating of PbI₂ and CH₃NH₃I in the 1 μ m long TiO₂ nanorod film results in J_{sc} of 20.92 mA/cm², V_{oc} of 869 mV, FF of 0.55, and PCE of 10.02%, which is higher than the previous result for the similar TiO₂ length⁹ because of the different coating procedure for the perovskite as mentioned previously. Compared to the ZnO

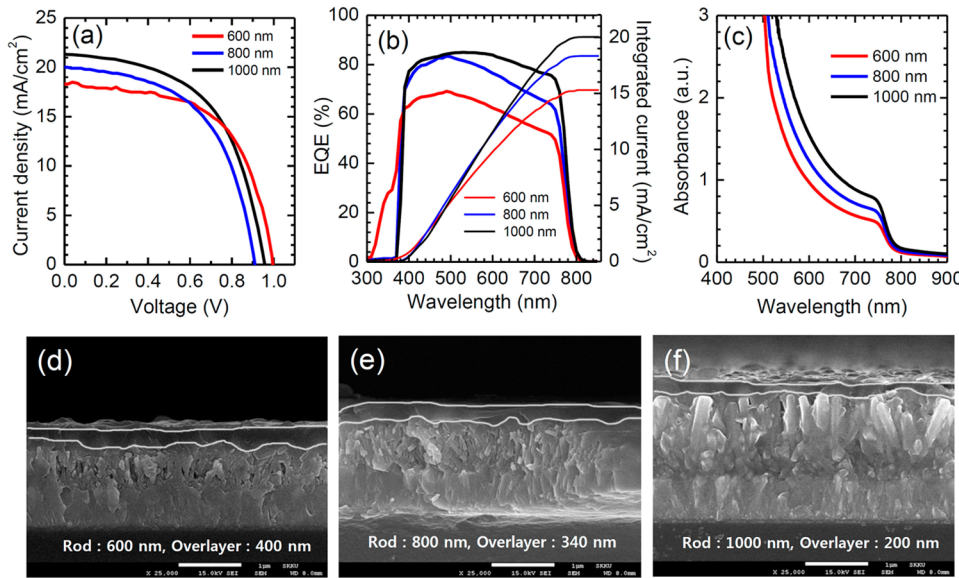


Figure 8. (a) Current density–voltage curves and (b) EQE spectra together with EQE data-based integrated current density for the perovskite solar cells based on ZnO nanorods with different lengths. (c) Absorption spectra of the perovskite coated ZnO nanorods with different lengths. Cross-sectional SEM images of perovskite-coated (d) 600, (e) 800, and (f) 1000 nm long ZnO nanorods. Different ZnO nanorod lengths were grown for 120 min (600 nm), 150 min (800 nm), and 180 min (1000 nm) in the 35 mM precursor solution.

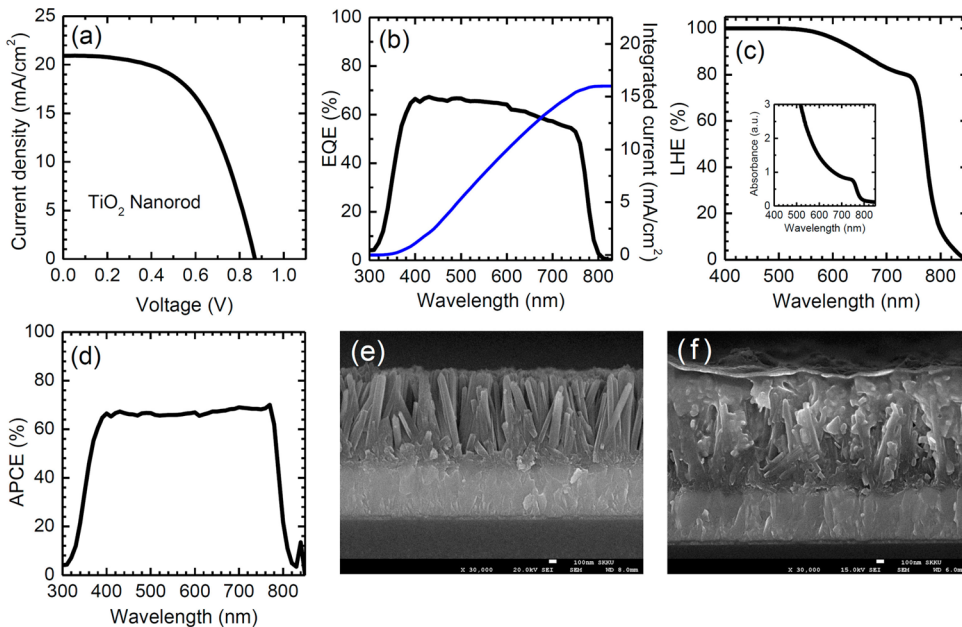


Figure 9. (a) Current density–voltage curve and (b) external quantum efficiency (EQE) spectrum together with EQE data-based integrated current density of the perovskite solar cell based on 1 μm long TiO_2 nanorods. Active area was 0.195 cm^2 . (c) Light harvesting efficiency (LHE) of the perovskite-coated TiO_2 nanorod film on FTO. Inset shows absorption spectrum. (d) Absorbed photon-to-current conversion efficiency (APCE) spectrum. Cross-sectional SEM images of (e) bare TiO_2 nanorod grown on FTO substrate and (f) full cell.

nanorod, the slightly lower PCE is due to lower V_{oc} , associated with lower conduction band position for the rutile TiO_2 structure and/or enhanced recombination. It is also noted that absolute EQE is lower in spite of high J_{sc} , and as a result, the integrated J_{sc} of about $16 \text{ mA}/\text{cm}^2$ is far lower than the measured J_{sc} at 1 sun illumination. In addition, APCE in Figure 9d is lower than that of ZnO (Figure 7d) in spite of similar LHE in Figure 9c. Because APCE can be described as the division of the EQE into its optical and electrical parts, difference in APCE at similar LHE underlines a difference in the electrical part. Thus, compared to high APCE in the ZnO

device, relatively lower APCE in the TiO_2 device suggests that charge collection limits the current for the TiO_2 nanorod-based perovskite solar cell.

Recombination behavior is investigated using the photo-voltage decay at open circuit. The time constant for recombination τ_{R} for the ZnO nanorod-based perovskite solar cell shows it to be almost 1 order of magnitude slower than that for the TiO_2 nanorod-based solar cell (Figure 10). A V_{oc} observed for the ZnO nanorod system that is slightly higher than that for the TiO_2 nanorod system is thus related to slower recombination characteristics. It is expected that recombination

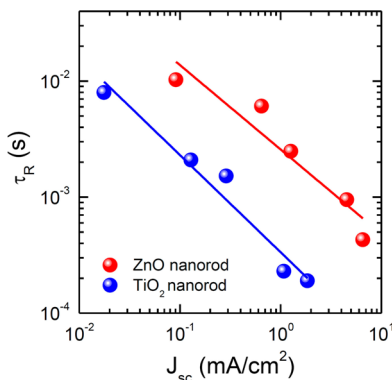


Figure 10. Comparison of time constant for charge recombination τ_R as a function of light intensity, represented by photocurrent density, for the ZnO nanorod-based perovskite solar cell and the TiO₂ nanorod-based solar cell.

behavior seems to be similar between ZnO and TiO₂ when no electron injection occurs. Thus, photoexcited electrons in the perovskite are likely to be injected to ZnO nanorod as evidenced by the difference in τ_R values.

Figure 11 compares time-limited photocurrent response under a monochromatic beam. The photocurrent signal for the

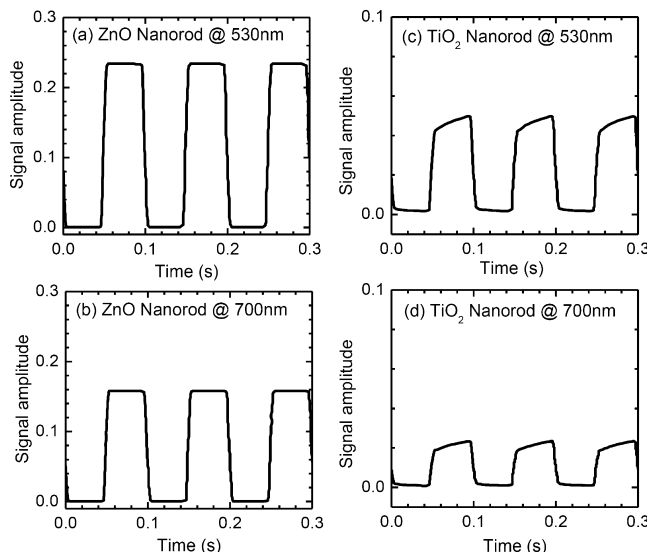


Figure 11. Time-limited photocurrent response at a monochromatic beam of 530 and 700 nm for (a, b) ZnO nanorod-based perovskite solar cell and (c, d) TiO₂ nanorod-based perovskite solar cell.

ZnO nanorod system is fully detected under 530 and 700 nm, whereas the signal detection is not completed for the TiO₂ nanorod system because the absolute signal amplitude for the TiO₂ nanorod system is merely 15–20% of that for the ZnO nanorod system despite similar photocurrent density observed for both systems. In addition, there are two pathways in collecting photoelectrons for the TiO₂ nanorod system: a fast and a very slow pathway. The very slow kinetics for collecting electrons is likely to limit full detection in the TiO₂ nanorod system, compared to the fast electron collection occurring through the very fast single pathway in the ZnO nanorod system. We found that a slight increase in photocurrent at slower scan in the $J-V$ measurement was observed for the TiO₂ device (data are not shown), which also confirms that the

charge collection limits the current for the TiO₂ device at faster times. Therefore, ZnO nanorod is an effective charge collection system in CH₃NH₃PbI₃ based perovskite solar cell.

CONCLUSION

We have fabricated a high-efficiency ZnO nanorod-based perovskite solar cell with PCE of over 11%. Diameter and length of the hexagonal ZnO nanorods were manipulated by controlling concentration of the precursor solution and immersion time. Two-step spin-coating of PbI₂ and CH₃NH₃I solutions led to void-filling with CH₃NH₃PbI₃ perovskite in ZnO nanorod film. The ZnO nanorod-based perovskite solar cell showed almost ideal EQE spectral shape with excellent matching of the calculated J_{sc} with the measured J_{sc} . Compared to a limited detection in charge collection due to slow charge collection rate and low APCE for the TiO₂ nanorod-based perovskite solar cell, the ZnO nanorod system showed fast saturation in charge collection, which indicates that ZnO nanorods are an effective charge collection system in CH₃NH₃PbI₃ based perovskite solar cells.

AUTHOR INFORMATION

Corresponding Author

*Tel: +82-31-290-7241. Fax: +82-31-290-7272. E-mail: npark@skku.edu.

Notes

The authors declare no competing financial interest.

ACKNOWLEDGMENTS

This work was supported by the National Research Foundation of Korea (NRF) grants funded by the Ministry of Science, ICT & Future Planning (MSIP) of Korea under Contracts NRF-2010-0014992, NRF-2012M1A2A2671721, NRF-2012M3A7B4049986 (Nano Material Technology Development Program), and NRF-2012M3A6A7054861 (Global Frontier R&D Program on Center for Multiscale Energy System).

REFERENCES

- (1) Kojima, A.; Teshima, K.; Shirai, Y.; Miyasaka, T. Organometal Halide Perovskites as Visible-Light Sensitizers for Photovoltaic Cells. *J. Am. Chem. Soc.* **2009**, *131*, 6050–6051.
- (2) Im, J.-H.; Lee, C.-R.; Lee, J.-W.; Park, S.-W.; Park, N.-G. 6.5% Efficient Perovskite Quantum-Dot-Sensitized Solar Cell. *Nanoscale* **2011**, *3*, 4088–4093.
- (3) Kim, H.-S.; Lee, C.-R.; Im, J.-H.; Lee, K.-B.; Moehl, T.; Marchioro, A.; Moon, S.-J.; Humphry-Baker, R.; Yum, J.-H.; Moser, J. E.; et al. Lead Iodide Perovskite Sensitized All-Solid-State Submicron Thin Film Mesoscopic Solar Cell with Efficiency Exceeding 9%. *Sci. Rep.* **2012**, *2*, 591.
- (4) Lee, M. M.; Teuscher, J.; Miyasaka, T.; Murakami, T. N.; Snaith, H. J. Efficient Hybrid Solar Cells Based on Meso-Superstructured Organometal Halide Perovskites. *Science* **2012**, *338*, 643–647.
- (5) Burschka, J.; Pellet, N.; Moon, S.-J.; Humphry-Baker, R.; Gao, P.; Nazeeruddin, M. K.; Grätzel, M. Sequential Deposition as a Route to High-Performance Perovskite-Sensitized Solar Cells. *Nature* **2013**, *499*, 316–319.
- (6) Liu, M.; Johnston, M. B.; Snaith, H. J. Efficient Planar Heterojunction Perovskite Solar Cells by Vapour Deposition. *Nature* **2013**, *501*, 395–398.
- (7) Park, N.-G. Organometal Perovskite Light Absorbers Toward a 20% Efficiency Low-Cost Solid-State Mesoscopic Solar Cell. *J. Phys. Chem. Lett.* **2013**, *4*, 2423–2429.

- (8) Snaith, H. J. Perovskites: The Emergence of a New Era for Low-Cost, High-Efficiency Solar Cells. *J. Phys. Chem. Lett.* **2013**, *4*, 3623–3630.
- (9) Kim, H.-S.; Lee, J.-W.; Yantara, N.; Boix, P. P.; Kulkarni, S. A.; Mhaisalkar, S.; Grätzel, M.; Park, N.-G. High Efficiency Solid-State Sensitized Solar Cell-Based on Submicrometer Rutile TiO₂ Nanorod and CH₃NH₃PbI₃ Perovskite Sensitizer. *Nano Lett.* **2013**, *13*, 2412–2417.
- (10) Qiu, J.; Qiu, Y.; Yan, K.; Zhong, M.; Mu, C.; Yan, H.; Yang, S. All-Solid-State Hybrid Solar Cells Based on a New Organometal Halide Perovskite Sensitizer and One-Dimensional TiO₂ Nanowire Arrays. *Nanoscale* **2013**, *5*, 3245–3248.
- (11) Dharani, S.; Mulmudi, H. K.; Yantara, N.; Thrang, P. T. T.; Park, N.-G.; Grätzel, M.; Mhaisalkar, S.; Mathews, N.; Boix, P. P. High Efficiency Electrospun TiO₂ Nanofiber Based Hybrid Organic-Inorganic Perovskite Solar Cell. *Nanoscale* **2014**, *6*, 1675–1679.
- (12) Kumar, M. H.; Yantara, N.; Dharani, S.; Grätzel, M.; Mhaisalkar, S.; Boix, P. P.; Mathews, N. Flexible, Low-Temperature, Solution Processed ZnO-Based Perovskite Solid State Solar Cells. *Chem. Commun.* **2013**, *49*, 11089–11091.
- (13) Bi, D.; Boschloo, G.; Schwarzmuller, S.; Yang, L.; Johansson, E. M. J.; Hagfeldt, A. Efficient and Stable CH₃NH₃PbI₃-Sensitized ZnO Nanorod Array Solid-State Solar Cells. *Nanoscale* **2013**, *5*, 11686–11691.
- (14) Greene, L. E.; Law, M.; Goldberger, J.; Kim, F.; Johnson, J. C.; Zhang, Y.; Saykally, R. J.; Yang, P. Low-Temperature Wafer-Scale Production of ZnO Nanowire Arrays. *Angew. Chem., Int. Ed.* **2003**, *42*, 3031–3034.
- (15) Greene, L. E.; Law, M.; Tan, D. H.; Montano, M.; Goldberger, J.; Somorjai, G.; Yang, P. General Route to Vertical ZnO Nanowire Arrays Using Textured ZnO Seeds. *Nano Lett.* **2005**, *5*, 1231–1236.
- (16) Huu, N. K.; Son, D.-Y.; Jang, I.-H.; Lee, C.-R.; Park, N.-G. Hierarchical SnO₂ Nanoparticle-ZnO Nanorod Photoanode for Improving Transport and Life Time of Photoinjected Electrons in Dye-Sensitized Solar Cell. *ACS Appl. Mater. Interfaces* **2013**, *5*, 1038–1043.
- (17) Jeong, W. S.; Lee, J. W.; Jung, S.; Yun, J. H.; Park, N.-G. Evaluation of External Quantum Efficiency of a 12.35% Tandem Solar Cell Comprising Dye-Sensitized and CIGS Solar Cells. *Sol. Energy Mater. Sol. Cells* **2011**, *95*, 3419–3423.
- (18) Kim, M.-J.; Lee, C.-R.; Jeong, W.-S.; Im, J.-H.; Ryu, T. I.; Park, N.-G. Unusual Enhancement of Photocurrent by Incorporation of Brönsted Base Thiourea Into Electrolyte of Dye-Sensitized Solar Cell. *J. Phys. Chem. C* **2010**, *114*, 19849–19852.
- (19) Kopidakis, N.; Benkstein, K. D.; van de Lagemaat, J.; Frank, A. J. Transport-Limited Recombination of Photocarriers in Dye-Sensitized Nanocrystalline TiO₂ Solar Cells. *J. Phys. Chem. B* **2003**, *107*, 11307–11315.
- (20) Vayssiers, L. Growth of Arrayed Nanorods and Nanowires of ZnO from Aqueous Solution. *Adv. Mater.* **2003**, *15*, 464–466.
- (21) Feng, X.; Feng, L.; Jin, M.; Zhai, J.; Jiang, L.; Zhu, D. Reversible Super-hydrophobicity to Super-hydrophilicity Transition of Aligned ZnO Nanorod Films. *J. Am. Chem. Soc.* **2004**, *126*, 62–63.
- (22) Chen, H.; Li, W.; Qin, H.; Liu, H.; Zhu, L. A General Deposition Method for ZnO Porous Films: Occlusion Electrosynthesis. *Electrochim. Acta* **2011**, *56*, 9459–9466.
- (23) Agrios, A. G.; Hagfeldt, A. Low-temperature TiO₂ Films for Dye-sensitized Solar Cells: Factors Affecting Energy Conversion Efficiency. *J. Phys. Chem. C* **2008**, *112*, 10021–10026.